

RESEARCH

Open Access



Injectable hydrogel encapsulating siMMP13 with anti-ROS and anti-apoptotic functions for osteoarthritis treatment

Zhongyin Ji^{1,3,5†}, Xiaobin Ren^{2†}, Jiayan Jin^{1,3†}, Xin Ye^{1,3†}, Hao Yu², Wenhan Fang⁴, Hui Li^{1,3}, Yihao Zhao^{1,3}, Siyue Tao^{1,3}, Xiangxi Kong^{1,3}, Jiao Cheng^{1,3}, Zhi Shan^{1,3}, Jian Chen^{1,3}, Qingqing Yao^{2*}, Fengdong Zhao^{1,3*} and Junhui Liu^{1,3*}

Abstract

Background Osteoarthritis (OA) is a degenerative joint disease characterized by the progressive degeneration of articular cartilage, leading to pain, stiffness, and loss of joint function. The pathogenesis of OA involves multiple factors, including increased intracellular reactive oxygen species (ROS), enhanced chondrocyte apoptosis, and disturbances in cartilage matrix metabolism. These processes contribute to the breakdown of the extracellular matrix (ECM) and the loss of cartilage integrity, ultimately resulting in joint damage and dysfunction. RNA interference (RNAi) therapy has emerged as a promising approach for the treatment of various diseases, including hATTR and acute hepatic porphyria. By harnessing the natural cellular machinery for gene silencing, RNAi allows for the specific inhibition of target genes involved in disease pathogenesis. In the context of OA, targeting key molecules such as matrix metalloproteinase-13 (MMP13), which plays a critical role in cartilage degradation, holds great therapeutic potential.

Results In this study, we developed an innovative therapeutic approach for OA using a combination of liposome-encapsulated siMMP13 and NG-Monomethyl-L-arginine Acetate (L-NMMA) to form an injectable hydrogel. The hydrogel served as a delivery vehicle for the siMMP13, allowing for sustained release and targeted delivery to the affected joint. Experiments conducted on destabilization of the medial meniscus (DMM) model mice demonstrated the therapeutic efficacy of this composite hydrogel. Treatment with the hydrogel significantly inhibited the degradation of cartilage matrix, as evidenced by histological analysis showing preserved cartilage structure and reduced loss of proteoglycans. Moreover, the hydrogel effectively suppressed intracellular ROS accumulation in chondrocytes, indicating its anti-oxidative properties. Furthermore, it attenuated chondrocyte apoptosis, as demonstrated by decreased levels of apoptotic markers.

[†]Zhongyin Ji, Xiaobin Ren, Jiayan Jin and Xin Ye contributed equally to this work.

*Correspondence:

Qingqing Yao
qingqingyao@wmu.edu.cn
Fengdong Zhao
zhaofengdong@zju.edu.cn
Junhui Liu
ljhzju@zju.edu.cn

Full list of author information is available at the end of the article



© The Author(s) 2024. **Open Access** This article is licensed under a Creative Commons Attribution-NonCommercial-NoDerivatives 4.0 International License, which permits any non-commercial use, sharing, distribution and reproduction in any medium or format, as long as you give appropriate credit to the original author(s) and the source, provide a link to the Creative Commons licence, and indicate if you modified the licensed material. You do not have permission under this licence to share adapted material derived from this article or parts of it. The images or other third party material in this article are included in the article's Creative Commons licence, unless indicated otherwise in a credit line to the material. If material is not included in the article's Creative Commons licence and your intended use is not permitted by statutory regulation or exceeds the permitted use, you will need to obtain permission directly from the copyright holder. To view a copy of this licence, visit <http://creativecommons.org/licenses/by-nc-nd/4.0/>.

Conclusion In summary, the injectable hydrogel containing siMMP13, endowed with anti-ROS and anti-apoptotic properties, may represent an effective therapeutic strategy for osteoarthritis in the future.

Keywords RNAi, Osteoarthritis, siMMP13, ROS, Apoptosis, Hydrogel, Liposome, Cartilage, Chondrocyte

Introduction

Osteoarthritis (OA) stands as a persistent degenerative condition affecting the entirety of joints, leading to both pain and a decline in mobility, ultimately diminishing the overall quality of life [1, 2]. The development of OA is intricately linked to a combination of mechanical and biochemical factors [3, 4]. Recognized risk factors include poor joint alignment or injury, obesity, genetic predisposition, and the natural process of aging [5, 6]. The pathogenesis of OA involves the orchestrated interplay of multiple signaling molecules, notably interleukin (IL-6, IL-1 β), MAPK, PI3K-Akt, and reactive oxygen species (ROS) [7–9]. These diverse signaling pathways independently contribute to an escalated production of matrix metalloproteinases (MMPs), a crucial step in the degradation of cartilage and the progression of OA symptoms [10, 11]. MMPs play a pivotal role in the deterioration of cartilage extracellular matrix (ECM) associated with OA, as they target and break down crucial structural elements such as type II collagen (Col2) and SRY sex determining region Y-box 9 (Sox9) [12, 13]. The imbalanced metabolism of ECM disrupts the chondrocyte niche and leads to apoptosis of chondrocytes [14, 15]. Additionally, the byproducts resulting from ECM degradation possess pro-inflammatory signaling properties, initiating a degenerative cycle that persists until the complete destruction of cartilage occurs [16, 17]. Given the heightened susceptibility of individuals to develop OA, there exists a potential window for early therapeutic intervention to impede the progression of the disease at its initial stages.

The current pharmaceutical approach to managing OA is primarily palliative, lacking clinically approved disease-modifying OA drugs (DMOADs) [18–20]. While there are five FDA-approved corticosteroids for intra-articular OA therapy, these interventions offer only temporary pain relief without addressing the underlying cause of the disease [21, 22]. Prolonged use of steroids is discouraged due to documented adverse effects, including cartilage volume loss over a two-year period when administered four times annually, heightened risk of joint replacement, and associations with chondrotoxicity [23, 24].

MMP13 emerges as a crucial proteolytic driver of cartilage loss in OA [25–27]. This is evident in reduced surgically-induced OA progression observed in MMP13 knockout mice and wild-type mice treated with broad MMP inhibitors [28, 29]. Unfortunately, clinical trials on MMP small molecule inhibitors, primarily explored for cancer treatment, have faced setbacks [30, 31]. These trials were halted due to musculoskeletal syndrome

(MSS)-related pain associated with the systemic delivery of small molecules that non-selectively inhibit multiple MMPs, some of which (MMP2, 3, 4, 7, and 9) play roles in normal tissue homeostasis [32, 33]. Developing selective small molecule inhibitors is challenging due to shared domains among collagenases and the homology of the catalytic site [34, 35]. Notably, a tested MMP13 inhibitor, PF152, showed promise in reducing lesion severity in a canine post-traumatic osteoarthritis (PTOA) model [36, 37]. However, it also exhibited nephrotoxicity, likely through off-target effects on the human organic anion transporter 3 [38, 39].

In light of these challenges, we have a hypothesis that selectively targeting MMP13 through RNAi therapy could prove to be an effective and safe approach for impeding the degenerative OA process [40]. This strategy aims to provide a targeted intervention without the systemic side effects encountered with broader MMP inhibitors, offering a potential avenue for advancing OA treatment.

Results

Design, synthesis, and characterization of composite hydrogel based on siRNA-containing liposome

To prevent the degradation of siRNAs by nucleases and ensure the delivery of siRNAs to the targeted sites, a liposome/siMMP13 loaded injectable hydrogel was developed. Here, the siMMP13 was encapsulated into a cationic lipid assisted mPEG-PLGA nanoparticle (liposome/siMMP13). TEM images showed that the liposome/siMMP13 exhibited monodisperse and spherical structure with an average diameter around 35.51 ± 10.77 nm (Fig. 1A and B). Additionally, the dynamic light scattering (DLS) data (Fig. 1C) showed that the hydrodynamic diameter of the liposome/siMMP13 was 95.99 ± 5.43 nm. Due to the presence of hydrophilic groups (PEG) in liposome, the hydrodynamic diameter of liposome in the colloidal state was much larger than that in the solid state [41]. And the positive potential of the liposome/siMMP13 (21.00 ± 5.55 mV) will be beneficial for liposome/siMMP13 cellular uptake (Fig. 1D) [42, 43]. The synthetic schemes of HA-PBA were showed in Fig. 1E. The successful of PBA modification of HA was confirmed by the ^1H NMR and FTIR spectra. Compared with the HA ^1H NMR spectra (Figure S1A), new characteristic absorption peaks between 7.49 ppm and 7.89 ppm were formed in HA-PBA, which were attributed to the benzene ring in the phenylboronic acid (Fig. 1F) [44, 45]. And the PBA substitution degree calculated from the

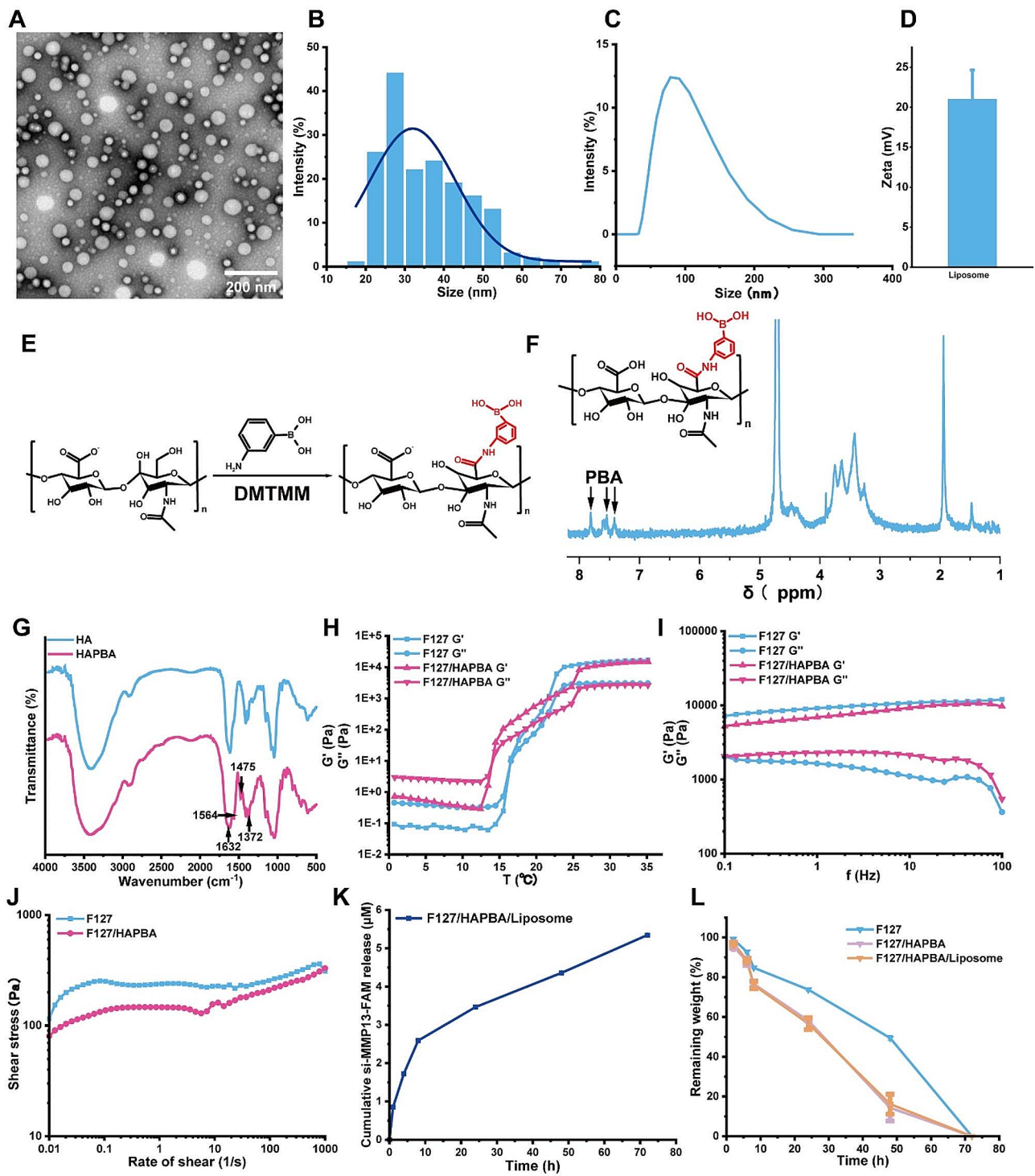


Fig. 1 (A) TEM images of liposome/siMMP13. (B) Size distribution of liposome/siMMP13. (C) DLS size measurements of liposome/siMMP13. (D) Zeta potential of liposome/siMMP13. (E) Synthesis scheme of HA-PBA. (F) ¹H NMR spectrum of HA-PBA. (G) FTIR spectrum of HA-PBA. Rheological tests of hydrogels by (H) temperature sweep and (I) frequency sweep. (J) F127 and F127/HAPBA hydrogels shear ramps at 37 °C. (K) siMMP13-FAM release behaviors from hydrogel in DPBS. (L) Degradation behaviors of F127, F127/HAPBA and F127/HAPBA/Liposome hydrogels immersed in DPBS solution for 3 days. Data are expressed as mean ± SD (n=3)

HA-PBA ^1H NMR data was nearly 48%. Moreover, the FTIR spectra (Fig. 1G) showed that the B-O absorption peak at 1372 cm^{-1} and C-B absorption peak at 1475 cm^{-1} [46, 47] were observed in HA-PBA, and the absorption peak at 1564 cm^{-1} and 1640 cm^{-1} were contributed to amide bond formed after PBA modification [44].

When the G' was smaller than G'' , the hydrogel showed liquid like state, and with the increase of temperature, the thermosensitive hydrogel's G' was higher than G'' , the samples underwent gelation and showed a solid-like state. The gelation transition temperature was detected at the junction between G' and G'' , the transition temperature of F127/HAPBA hydrogel was $13.96\text{ }^\circ\text{C}$, which was slightly lower than that of F127 hydrogel ($16.39\text{ }^\circ\text{C}$) (Fig. 1H). Both F127 and F127/HAPBA hydrogels showed a higher storage modulus (G') than loss modulus (G'') over a frequency range between 0.1 and 100 rad/s, indicating solid-like behaviors and good elastic characters of hydrogel. Moreover, the F127 hydrogel showed higher G' and lower G'' than F127/HAPBA hydrogel, indicating F127 hydrogel had better mechanical property. The F127 hydrogel showed higher shear stress than that of F127/HAPBA hydrogel with the shear rate between 0.01 and 1000 s^{-1} (Fig. 1J). We conducted peristaltic scanning using a rheometer at shear rates ranging from 0.01 s^{-1} to 1000 s^{-1} at $25\pm 0.2\text{ }^\circ\text{C}$. As shown in Figure S1, both hydrogels showed typical shear thinning behavior, and the viscosity decreases with the increase of shear rate. The shear viscosity of F127/HAPBA hydrogel was slightly lower than that of F127 hydrogel. These were conformed to the standard that the shear viscosity of hydrogel for intraarticular injection should not be less than $20,000\text{ mPa}\cdot\text{s}$ under the shear rate of 0.01 s^{-1} [48, 49]. In order to study the loading efficiency of siMMP13 in the liposome and the release of siMMP13 in the injectable hydrogel system, we customized siMMP13-FAM for subsequent experiments. The loading efficiency of siMMP13-FAM in liposome was 95.64%, and the standard curve of siMMP13-FAM was showed on Figure S1B. The release behaviors of siMMP13-FAM in hydrogel which was shown in the following Fig. 1K. Similarly to the degradation behaviors, the hydrogel released all of the siMMP13-FAM within 3 days, with a total release of nearly $5.5\text{ }\mu\text{M}$ siMMP13-FAM. The real-time release amount was nearly $0.88\text{ }\mu\text{M}$ at each time point.

We also measured the degradation behaviors of F127, F127/HA-PBA and F127/HAPBA/liposome hydrogels in a period of 72 h (Fig. 1L). Similar degradation profiles were observed between F127/HAPBA and F127/HAPBA/liposome hydrogels, while the F127 hydrogel showed a relative lower degradation rate in the period of 72 h. The change in the degradation behaviors among three types of hydrogels may be due to the addition of HA-PBA and liposome nanoparticles weakened the F127

physical network, which was consistent with the rheological results.

The liposome-based siRNA delivery system restores chondrocyte chondrogenic ability during inflammation

In clinical practice, many OA patients seek surgical treatment. Recent studies have shown that OA patients have abnormal anabolism and catabolism of cartilage matrix, especially MMP13. To investigate this, cartilage samples were collected from OA patients and trauma patients as a negative control (NC). Immunohistochemical staining of MMP13 revealed a significant upregulation in OA patients compared to the NC group (Fig. 2A and B). A designed liposome-encapsulated murine siMMP13 demonstrated optimal knockdown efficiency in primary chondrocytes, particularly at higher concentrations (Fig. 2C). Following IL-1 β stimulation, a concentration of 50 exhibited favorable therapeutic effects as determined by CCK-8 assays on primary chondrocytes (Figure S2A). This concentration significantly downregulated MMP13 without notable effects on matrix metabolism related aggrecan, Sox9, and MMP3 (Fig. 2D). Protein analysis further confirmed the effective knockout of MMP13 in chondrocytes post-inflammatory stimulation at the concentration of 50. Although higher concentrations of liposomes also available achieved MMP13 knockdown, they adversely affected the expression of aggrecan and Sox9 (Fig. 2E). Subsequent high-density cartilage culture experiments, including Alcian blue, safranin O and fast green, and toluidine blue staining, demonstrated that IL-1 β stimulation restrained the in vitro chondrogenic ability of cartilage. However, treatment with liposome-encapsulated siMMP13 significantly rescued this effect, highlighting the therapeutic potential of the developed siRNA delivery system (Fig. 2F).

The composite hydrogel effectively alleviates inflammation in cartilage and rescues the degradation of the cartilage matrix

NG-monomethyl-L-arginine acetate (L-NMMA) serves as a cell-permeable competitive inhibitor of nitric oxide synthase (NOS) and has been explored as a potential therapeutic agent for OA. Our investigation focused on its impact on chondrocytes following inflammatory stimulation, pinpointing an effective concentration of 0.5% (Figure S2B). Western blot (WB) analyses revealed that, relative to the IL-1 β -stimulated group, treatment with the composite hydrogel significantly downregulated the expression of iNOS, TNF- α , MMP13, and MMP3, while upregulating aggrecan and Sox9. In contrast, methylprednisolone (MP) reduced MMP13 and MMP3 without significantly affecting iNOS and TNF- α ; however, it negatively influenced the expression of aggrecan and Sox9 (Fig. 3A). qPCR results further demonstrated

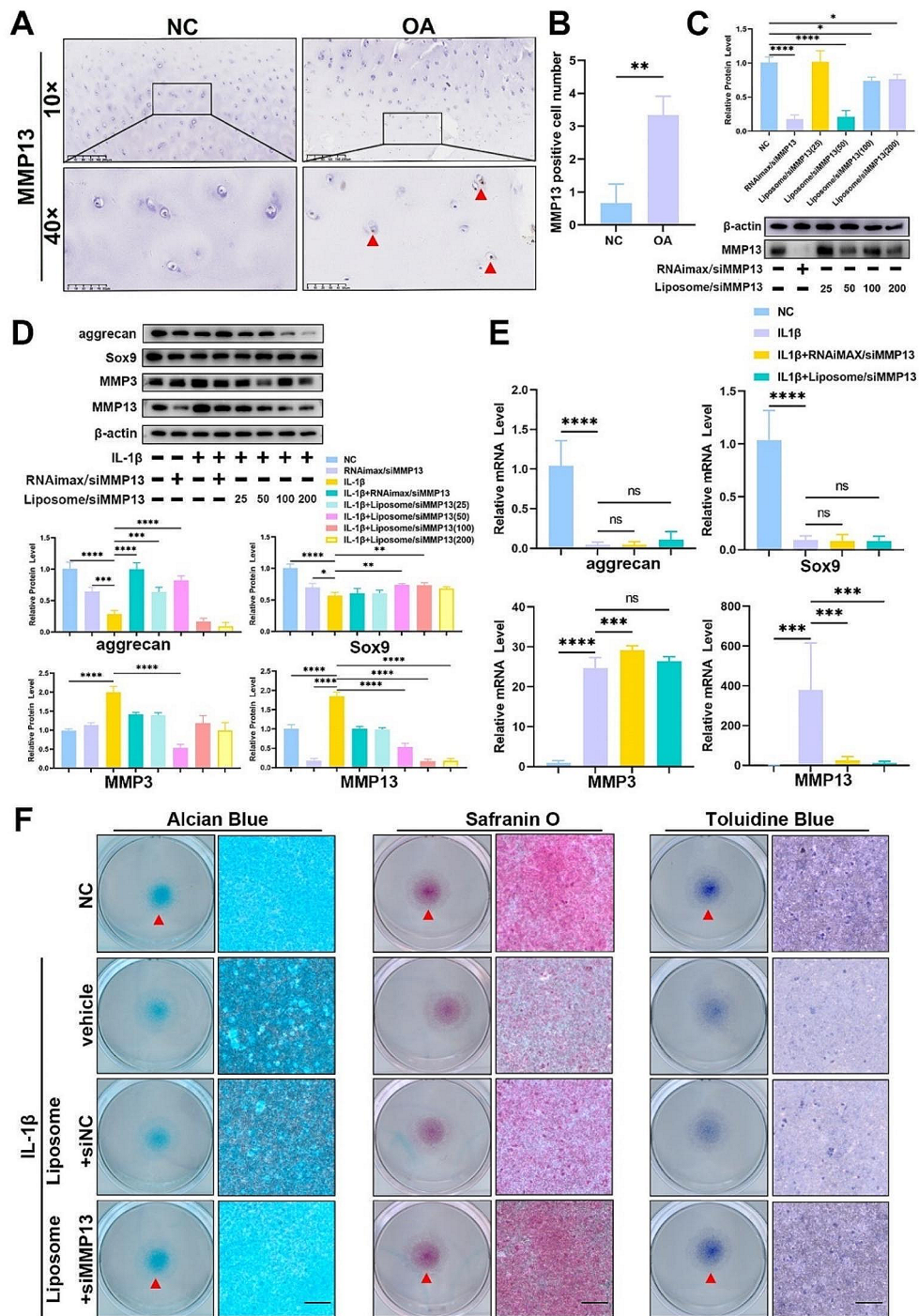


Fig. 2 (A) Representative IHC of MMP13 from human tissues of OA patients and non-OA patients. Scale bar, 50 μ m (10x), 200 μ m (40x). Statistical analysis (n=3) was presented in (B). (C) WB validation of MMP13 knockdown effect by liposome-encapsulated siRNA at different concentrations in chondrocytes (n=4). (D) WB validation of aggrecan, Sox9, Adams5, MMP13, and MMP3 expression levels in chondrocytes post-treatment (n=4). (E) Real-time Quantitative PCR (qPCR) validation of aggrecan, Sox9, MMP13, and MMP3 expression levels in chondrocytes post-treatment (n=6). (F) Chondrocytes were subjected to Alcian blue, Safranin O, and Toluidine Blue staining after treatment and cultured at high density. Scale bar, 100 μ m. (ns, no significance, * P <0.05, ** P <0.01, *** P <0.005, **** P <0.001)

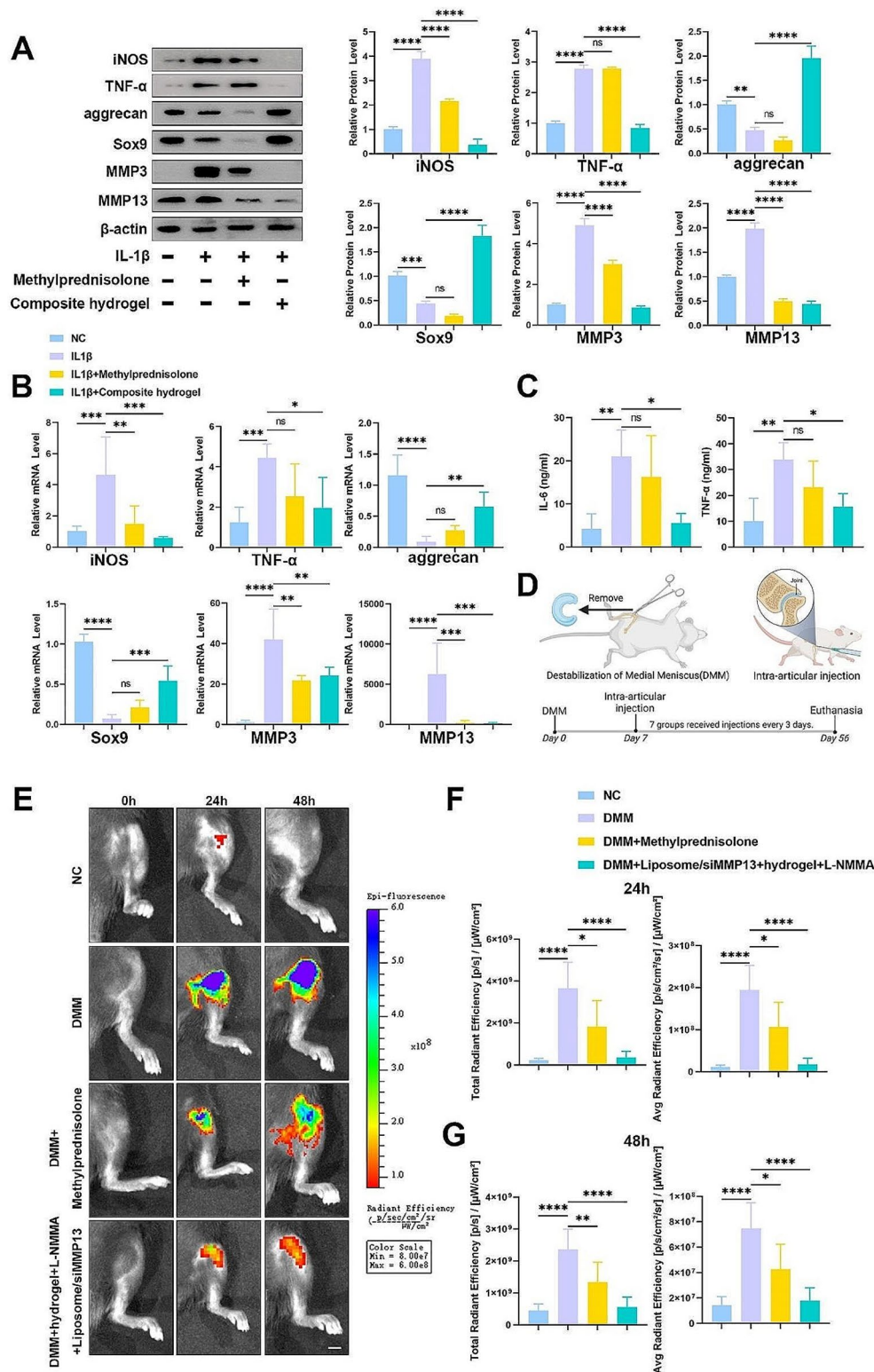


Fig. 3 (A) WB validation of iNOS, TNF- α , aggrecan, Sox9, Adamts5, MMP13, and MMP3 expression levels in chondrocytes after treatment with methylprednisolone and composite hydrogel ($n=4$). (B) qPCR validation of iNOS, TNF- α , aggrecan, Sox9, MMP13, and MMP3 expression levels in chondrocytes after treatment with methylprednisolone and composite hydrogel ($n=6$). (C) ELISA analysis of IL-6 and TNF- α in the supernatant of chondrocytes post-treatment. ($n=6$). (D) Schematic diagram of DMM modeling and knee joint injection. (E) Live imaging of MMP 680 fluorescent probe injected into mouse knee joints at 0, 24, and 48 h. Scale bar, 2 mm. The total fluorescence intensity and average fluorescence intensity at 24 h and 48 h were presented in (F) and (G). Data are expressed as mean \pm SD ($n=6$). (ns, no significance, * $P < 0.05$, ** $P < 0.01$, *** $P < 0.005$, **** $P < 0.001$)

that, compared to the IL-1 β -stimulated group, treatment with the composite hydrogel significantly suppressed the expression of inflammatory-related genes iNOS and TNF- α . Simultaneously, it markedly upregulated matrix synthesis-related markers aggrecan and Sox9 and significantly downregulated matrix degradation indicators MMP13 and MMP3. The therapeutic efficacy surpassed that of methylprednisolone (Fig. 3B). Subsequently, ELISA assays on the cell culture medium indicated that composite hydrogel treatment substantially diminished the expression levels of iNOS and TNF- α , whereas methylprednisolone exhibited no discernible therapeutic effects (Fig. 3C). In vitro high-density chondrocyte culture also unveiled the significant impact of IL-1 β stimulation on chondrocyte proliferation. While the methylprednisolone treatment group modestly alleviated this effect, the addition of the composite hydrogel demonstrated a pronounced rescuing effect, restoring chondrocyte proliferation to a level akin to the NC group (Figure S3). Moving forward, we subjected wild-type (WT) mice to destabilization of the medial meniscus (DMM) surgery [50, 51], followed by intra-articular injection into the knee joint (Fig. 3D). After 8 weeks of treatment, living images showcased a noteworthy reduction in knee joint MMP signal intensity in the composite hydrogel-treated group compared to both the DMM group and the methylprednisolone treatment group. This trend persisted 24 h and 48 h after contrast agent injection (Fig. 3E, F and G).

The composite hydrogel effectively delays the progression of osteoarthritis, preserving the integrity of the cartilage

To evaluate the therapeutic impact of the composite hydrogel on osteoarthritis (OA) prognosis, we utilized WT mice, categorizing them into seven groups: NC (sham surgery), DMM (OA modeling), DMM with hydrogel injection, DMM with hydrogel+L-NMMA injection, DMM with hydrogel+L-NMMA+Liposome loaded with NC siRNA injection, DMM with methylprednisolone (MP) injection, and DMM with hydrogel+L-NMMA+Liposome loaded with siMMP13 injection (composite hydrogel). After 8 weeks, organ samples underwent hematoxylin and eosin (H&E) staining, indicating consistent biocompatibility and low biotoxicity of the composite hydrogel (Figure S4). Micro-CT analysis of knee joints revealed NC joints displayed smooth surfaces and larger joint cavities, while DMM joints exhibited increased porosity, rough surfaces, extensive spurs, and reduced joint cavities. The hydrogel-treated groups, either alone or in combination with L-NMMA or NC siRNA-loaded Liposomes, exhibited modest rescue effects. In contrast, the MP group demonstrated a reduction in surface fissures and spurs, maintaining the height of the joint cavity. Remarkably,

the composite hydrogel-treated group presented notably smooth joint surfaces, minimal spurs, and a nearly unaffected joint cavity (Fig. 4A). Statistical analysis of DMM modeling highlighted significant reductions in bone volume fraction (BV/TV), trabecular number (Tb.N), and trabecular thickness (Tb.Th), coupled with increased trabecular separation (Tb.Sp). This indicated microstructural damage, reduced cartilage integrity, increased spur formation, and enhanced porosity. The hydrogel, along with the L-NMMA and NC siRNA-loaded Liposome groups, showed no significant rescue effects. Conversely, both MP and composite hydrogel treatment groups demonstrated significant therapeutic effects (Fig. 4B, C, D and E). Bone mineral density (BMD) and cortical thickness on the distal side showed no significant intergroup differences, suggesting minimal impact on cortical bone. However, the ratio of bone surface area to bone volume (BS/BV) increased post-DMM, indicating heightened cortical bone porosity. Remarkably, the hydrogel treatment significantly mitigated this effect (Fig. 4F, G and H).

The macroscopic images illustrated the status of the femoral condyles. In NC group, the bone surface exhibited a smooth contour without aberrant protuberances or fascial proliferation. Conversely, the DMM group presented uneven bone surfaces, accompanied by extensive connective tissue proliferation and the formation of osteophytes. The injection of hydrogel, hydrogel+L-NMMA, and hydrogel+L-NMMA+Liposome loaded with NC siRNA exhibited insufficient rescue effects. The bone surfaces remained irregular, featuring substantial fascial proliferation and localized osteophyte formation. The MP treatment group manifested a moderately smoother joint appearance, albeit with some anomalous growth. Notably, the composite hydrogel treatment group demonstrated superior therapeutic efficacy, enhancing joint smoothness, diminishing fascial proliferation, and averting osteophyte formation (Fig. 5A). Histological staining with H&E, Safranin O/Fast Green, Alcian Blue, and Manson's staining revealed considerable structural impairment and cartilage loss in the DMM group compared to the NC group. Treatment groups, including hydrogel injection, hydrogel+L-NMMA injection, and hydrogel+L-NMMA+Liposome loaded with NC siRNA injection, demonstrated limited therapeutic effectiveness, presenting noticeable cartilage defects and matrix loss. The MP treatment group maintained cartilage morphology but still displayed significant matrix loss. In contrast, the composite hydrogel injection group exhibited a more effective treatment outcome, preserving cartilage morphology without evident matrix loss (Fig. 5B, C and D, Figure S5). OARIS scores delineated heightened osteoarthritic severity in the DMM group and the subsequent four treatment groups relative to the NC group. Nevertheless, the composite hydrogel treatment group

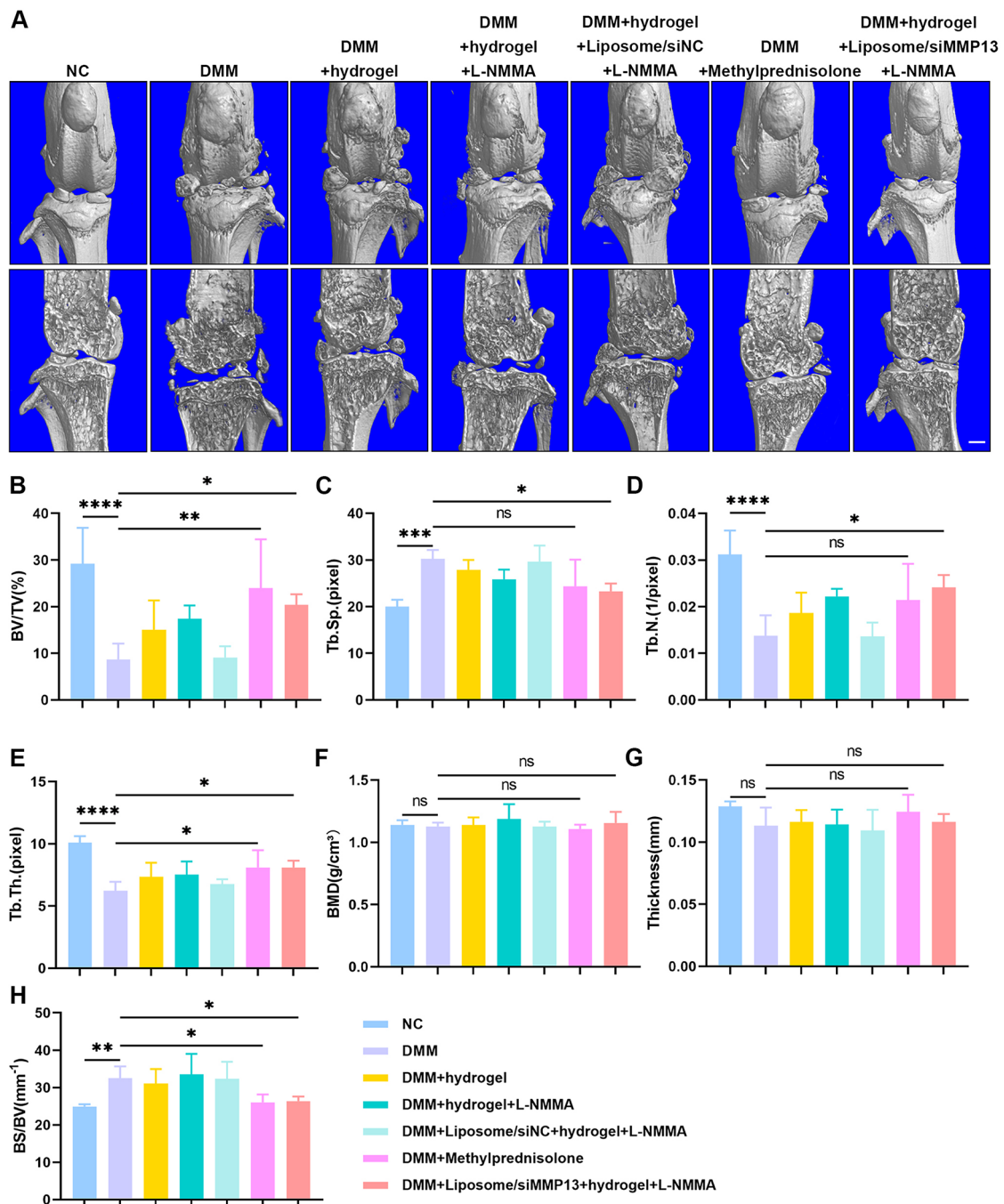


Fig. 4 (A) The 3D reconstructed images and coronal section images obtained from micro-CT scans of different groups. Scale bar, 1 mm. (B) Bone volume fraction (BV/TV). (C) Trabecular separation (Tb. sp.). (D) Trabecular number (Tb. n.). (E) Trabecular thickness (Tb. Th.). (F) Bone mineral density (BMD). (G) Cortical bone thickness. (H) Bone surface-to-volume ratio (BS/BV). Data are expressed as mean ± SD (n=6). (ns, no significance, *P<0.05, **P<0.01, ***P<0.005, ****P<0.001)

exhibited no significant difference, suggesting a superior treatment outcome. Mankin scores revealed a substantial increase in scores for the DMM group and the subsequent five treatment groups compared to the control group. However, in contrast to the DMM group, both the MP and composite hydrogel treatment groups displayed a notable score reduction, with the composite hydrogel

treatment group demonstrating a more pronounced and consistent downward trend (Fig. 5E and F). Furthermore, ELISA of interleukin-6 (IL-6) and tumor necrosis factor-alpha (TNF-α) concentrations in mice serum unveil a decreasing trend in the composite hydrogel group compared to the DMM group. Nonetheless, no statistically significant difference was discerned, possibly owing to

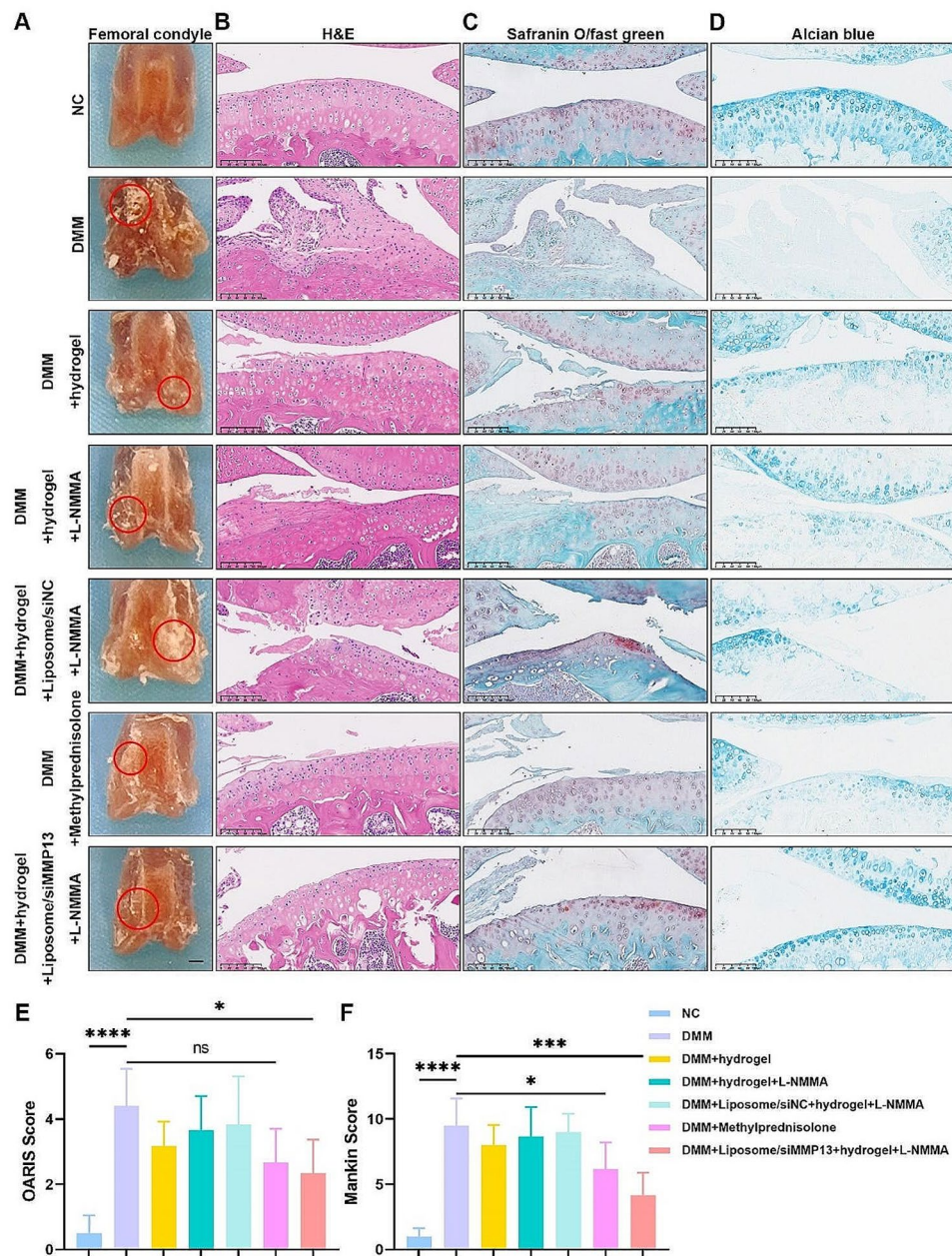


Fig. 5 (A) Representative gross images of femoral condyles. Scale bar, 1 mm. (B) Representative H&E staining. Scale bar, 200 μ m. (C) Representative Safranin O/Fast Green staining. Scale bar, 200 μ m. (D) Representative Alcian blue staining. Scale bar, 200 μ m. (E) Osteoarthritis Research Society International (OARIS) scores of articular cartilages in seven groups. (F) Mankin scores of articular cartilages in seven groups. Data are expressed as mean \pm SD ($n=6$). (ns, no significance, $*P<0.05$, $**P<0.01$, $***P<0.005$, $****P<0.001$)

the localized nature of the osteoarthritic lesions induced by DMM, resulting in subtle changes in systemic inflammatory factors (Figure S6).

The composite hydrogel effectively maintains the metabolic stability of the cartilage matrix

To further explore the efficacy and mechanism of the composite hydrogel, knee joint sections were obtained for immunohistochemistry (IHC) and immunofluorescence (IF) analyses of markers related to cartilage matrix

anabolism and catabolism. IHC staining for MMP13 revealed a significant upregulation in the joint cartilage region of the DMM group compared to the NC group. The injection of hydrogel, hydrogel+L-NMMA, hydrogel+L-NMMA+Liposome loaded with NC siRNA, and the MP treatment group also exhibited notable increases in MMP13, indicating enhanced cartilage matrix degradation. In contrast, the composite hydrogel treatment group showed a significant downregulation of MMP13 in the cartilage matrix (Fig. 6A and D). IHC staining for

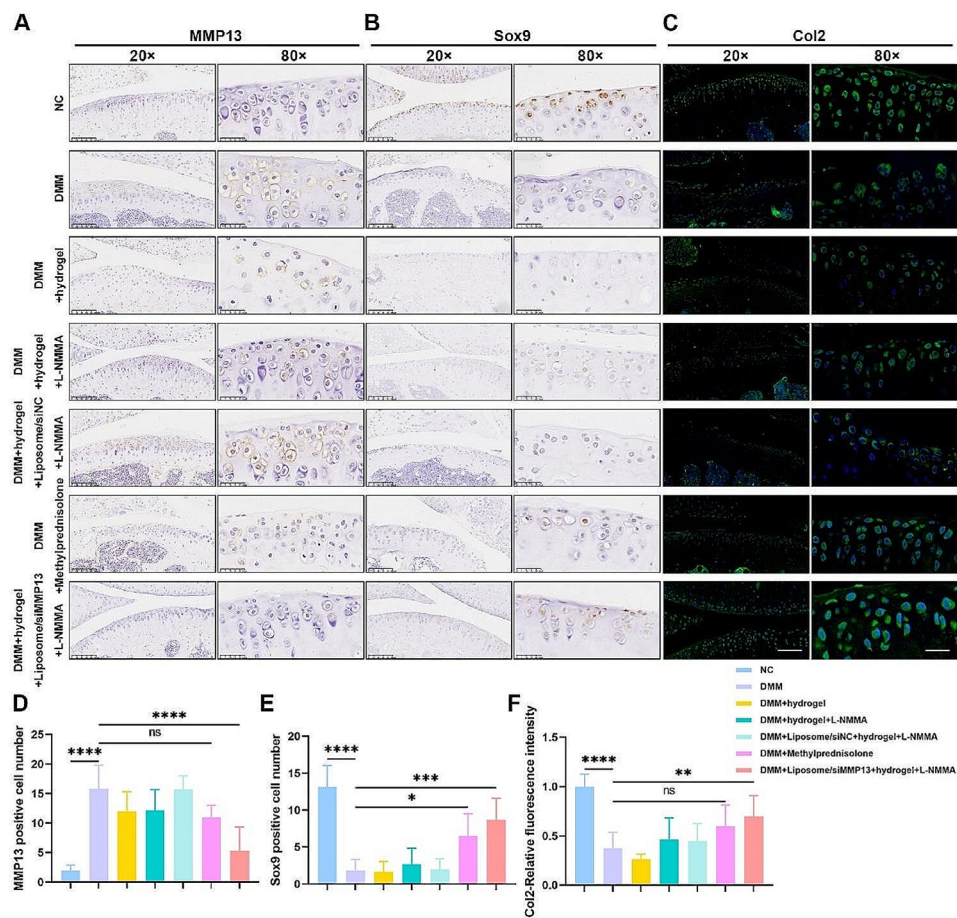


Fig. 6 (A) Representative IHC staining of MMP13 from the knee joint of mice in different groups. Quantitative analysis presented in (D). (B) Representative IHC staining of Sox9 from the knee joint of mice in different groups. Quantitative analysis presented in (E). (C) Representative IF staining of Col2 from the knee joint of mice in different groups. Quantitative analysis presented in (F). Data are expressed as mean \pm SD ($n = 6$). Scale bar, 200 μ m (20 \times), 50 μ m (80 \times). (ns, no significance, * $P < 0.05$, ** $P < 0.01$, *** $P < 0.005$, **** $P < 0.001$)

MMP3 displayed a similar trend (Figure S7). IHC of Sox9 revealed a significant downregulation in all groups compared to the NC group. However, when compared to the DMM group, both the MP treatment group and the composite hydrogel treatment group exhibited an upregulation of Sox9, with a more pronounced rescue effect in the composite hydrogel group (Fig. 6B and E). IF staining for Col2 also demonstrated a downregulation in all treatment groups compared to the NC group. Interestingly, the composite hydrogel treatment group showed a rescue effect compared to the DMM group, while the MP treatment group did not exhibit a significant difference (Fig. 6C and F).

The composite hydrogel can rescue the gene expression of chondrocytes under inflammatory stimulation

To explore the specific mechanism of the composite hydrogel treatment, we cultured chondrocytes in vitro, categorizing them into NC, IL-1 β stimulation, IL-1 β stimulation followed by methylprednisolone treatment,

and IL-1 β stimulation followed by composite hydrogel treatment groups. Subsequently, we conducted transcriptome sequencing. After IL-1 β stimulation, chondrocytes displayed the upregulation of 1088 genes and the downregulation of 995 genes. Additionally, 1680 transcripts were upregulated, while 1402 transcripts were downregulated. Following treatment with the composite hydrogel, 187 genes exhibited upregulation, 125 genes showed downregulation (Figure S8A). Protein-protein interaction (PPI) analysis unveiled key protein clusters involving inflammation-related genes such as MMP13, IL6, Ccl2, matrix metabolism-related gene Col2a1, oxidative stress-related gene Nos2, and apoptosis-related gene Bcl (Figure S8B). Gene Ontology (GO) analysis indicated that differentially expressed genes across the four groups were enriched in processes like matrix metabolism, ossification, and hypoxic response (Figure S8C). Kyoto Encyclopedia of Genes and Genomes (KEGG) analysis demonstrated that differentially expressed pathways

among the four groups were associated with apoptosis, phagosome, lysosome, ferroptosis (Figure S8D).

After exposure to inflammatory factor, chondrocytes experienced a notable increase in the transcription levels of inflammation-related genes, including *IL13ra2*, *Steap4*, matrix catabolism-related *MMP3*, reactive oxygen species-related *Nos2*, and apoptosis-related *Zc3h12a* (Fig. 7A). Treatment with the composite hydrogel resulted in the downregulation of *Nos2*, *IL13ra2*, and apoptosis-related gene *Rnd1*, while the transcription levels of cartilage formation-related molecules *Omd* and *Itgbl1* were upregulated (Fig. 7B). GO analysis revealed significant alterations in chondrocyte apoptosis and apoptosis inhibition processes following inflammatory stimulation, suggesting an elevated level of chondrocyte apoptosis (Fig. 7C). However, after treatment with the composite hydrogel, the expression of genes related to the apoptosis process significantly decreased, indicating that the therapeutic effect of the composite hydrogel may involve rescuing chondrocyte apoptosis (Fig. 7D). KEGG analysis indicated notable changes in the PI3K-Akt signaling pathway and MAPK pathway within chondrocytes after inflammatory stimulation (Fig. 7E). Following treatment with the composite hydrogel, modifications were observed in the PI3K-Akt signaling pathway (Fig. 7F), suggesting that the therapeutic effect of the composite hydrogel may be mediated through these signaling pathways. Subsequently, WB demonstrated a significant increase in the phosphorylation levels of PI3K and Akt after treatment with the composite hydrogel (Fig. 7G). Meanwhile, transcriptome sequencing results suggested that other classic pathways widely studied in OA showed no significant differences (Figure S9).

The composite hydrogel exhibits anti-ROS activity and inhibits chondrocyte apoptosis

To further substantiate our findings, we conducted *in vitro* cultivation of chondrocytes followed by flow cytometry analysis. The results demonstrated a substantial increase in intracellular ROS levels in chondrocytes upon stimulation with inflammatory factors. Notably, both the MP treatment group and the composite hydrogel treatment group showed significant inhibition of intracellular ROS levels (Fig. 8A and B). The use of ROS fluorescent probes further validated the elevated ROS levels in chondrocytes under inflammatory conditions. Importantly, the MP treatment demonstrated a modest inhibitory effect, whereas the composite hydrogel treatment led to a pronounced decrease in intracellular ROS levels (Fig. 8C). Subsequently, we utilized human tissue specimens to conduct IHC staining of the anti-apoptotic marker BCL2A1. The significant downregulation of BCL2A1 levels in knee joint cartilage from OA patients compared to the NC group indicated an escalation in

chondrocyte apoptosis (Fig. 8D and E). Flow cytometry analysis of cultured chondrocytes unveiled an increase in apoptosis under inflammatory stimulation, while the composite hydrogel treatment exhibited a notable inhibition of apoptosis (Fig. 8F and G). Proteins associated with apoptosis, such as BCL2, exhibited a decrease after inflammatory stimulation but an increase after composite hydrogel treatment. Conversely, pro-apoptotic proteins BAX and Cleaved caspase-3 displayed an upregulation following inflammatory stimulation but a downregulation after composite hydrogel treatment (Fig. 8H). Scanning electron microscopy analysis of knee joint cartilage illustrated that, in comparison to the NC group, chondrocytes in the DMM group displayed fragmented cell nuclei and unclear or disappeared organelle structures. The MP treatment group exhibited numerous apoptotic bodies resembling vacuoles with a trend of nuclear fragmentation. In contrast, the composite hydrogel treatment group showcased a superior therapeutic effect, with chondrocyte nuclei maintaining a more normal morphology and fewer apoptotic bodies (Fig. 8I). IHC analysis of BCL2A1 indicated a significant downregulation of BCL2A1 expression in the DMM group compared to the NC group. The subsequent four treatment groups displayed no discernible rescue effect, while the composite hydrogel treatment group exhibited a significant increase in BCL2A1 expression (Fig. 8J).

Discussion

OA is a polygenic degenerative joint disorder characterized by the progressive degradation of articular cartilage, leading to symptomatic manifestations such as pain, stiffness, and functional impairment [5]. The pathogenesis of OA involves a multifaceted interplay of biomechanical stress, genetic predisposition, and biochemical alterations within the local joint microenvironment [1]. The clarification of molecular pathways driving OA pathogenesis, as illuminated in this investigation, yields invaluable insights into prospective therapeutic targets for disease intervention. Elevated intracellular reactive oxygen species (ROS), intensified chondrocyte apoptosis, and perturbations in cartilage matrix metabolism are pivotal processes implicated in OA advancement [7]. These mechanisms collectively precipitate extracellular matrix (ECM) degradation and cartilage structural compromise, culminating in joint deterioration and functional compromise. Currently, in clinical practice, there is a lack of treatment methods for OA with clear efficacy.

RNA interference therapy has emerged as a promising avenue for the treatment of various diseases [52]. By exploiting the natural cellular mechanism of gene silencing, RNAi therapy offers a targeted approach to modulate disease-associated pathways at the molecular level [53, 54]. In the context of OA, RNAi therapy holds immense

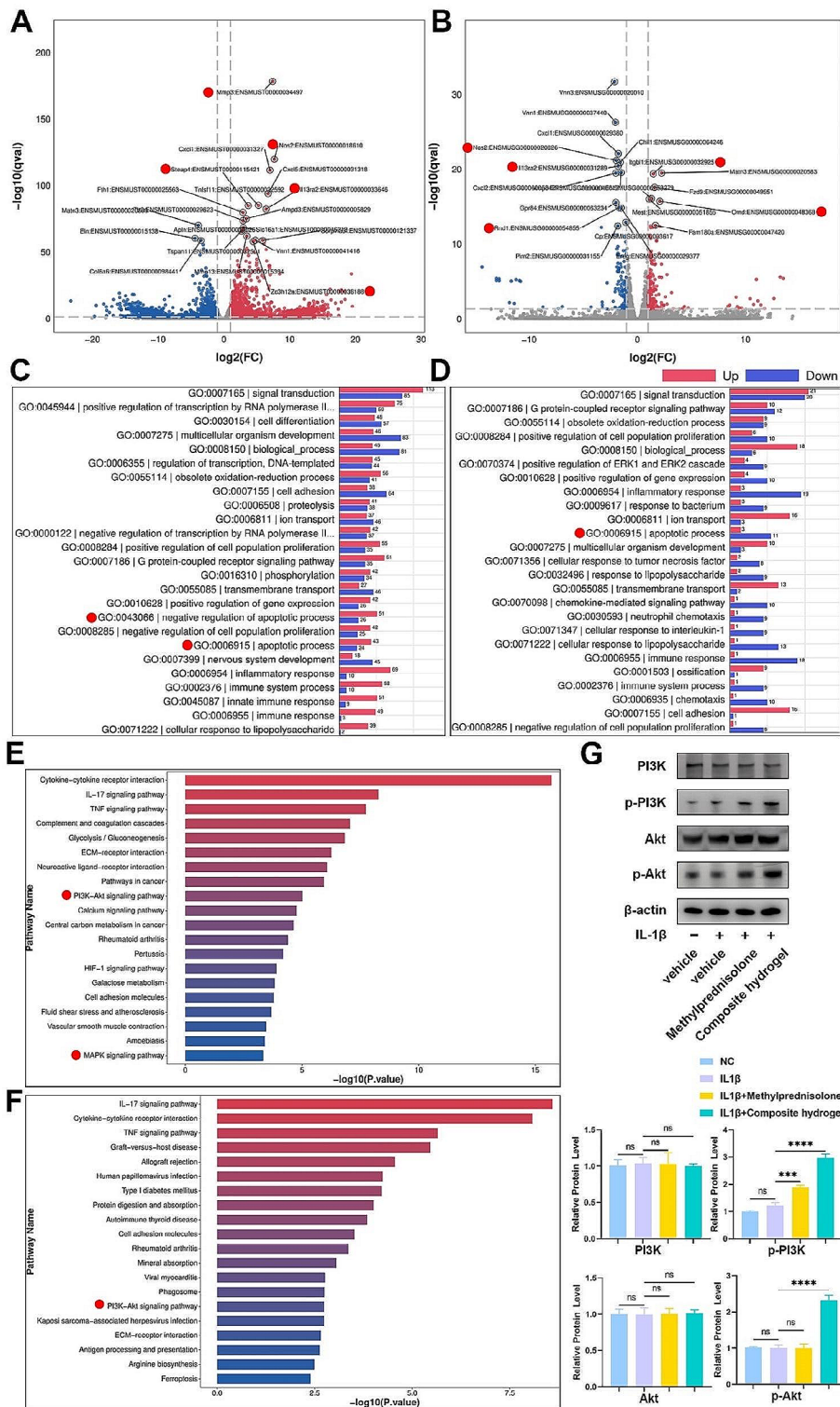


Fig. 7 (A) Volcano plots of differential gene expression in chondrocytes before and after stimulation by IL-1 β . (B) Volcano plot of differential gene expression in chondrocytes responding to IL-1 β stimulation before and after treatment with composite hydrogel. (C) Bar chart of GO enrichment for up- and down-regulated genes in chondrocytes before and after stimulation by IL-1 β . (D) Bar chart of GO enrichment for up- and down-regulated genes in chondrocytes responding to IL-1 β stimulation before and after treatment with composite hydrogel. (E) Top 20 of KEGG enrichment of pathway in chondrocytes before and after stimulation by IL-1 β . (F) Top 20 of KEGG enrichment of pathway in chondrocytes responding to IL-1 β stimulation before and after treatment with composite hydrogel. (G) WB of PI3K, p-PI3K, Akt, p-Akt, and β -actin ($n=4$). (ns, no significance, * $P < 0.05$, ** $P < 0.01$, *** $P < 0.005$, **** $P < 0.001$)

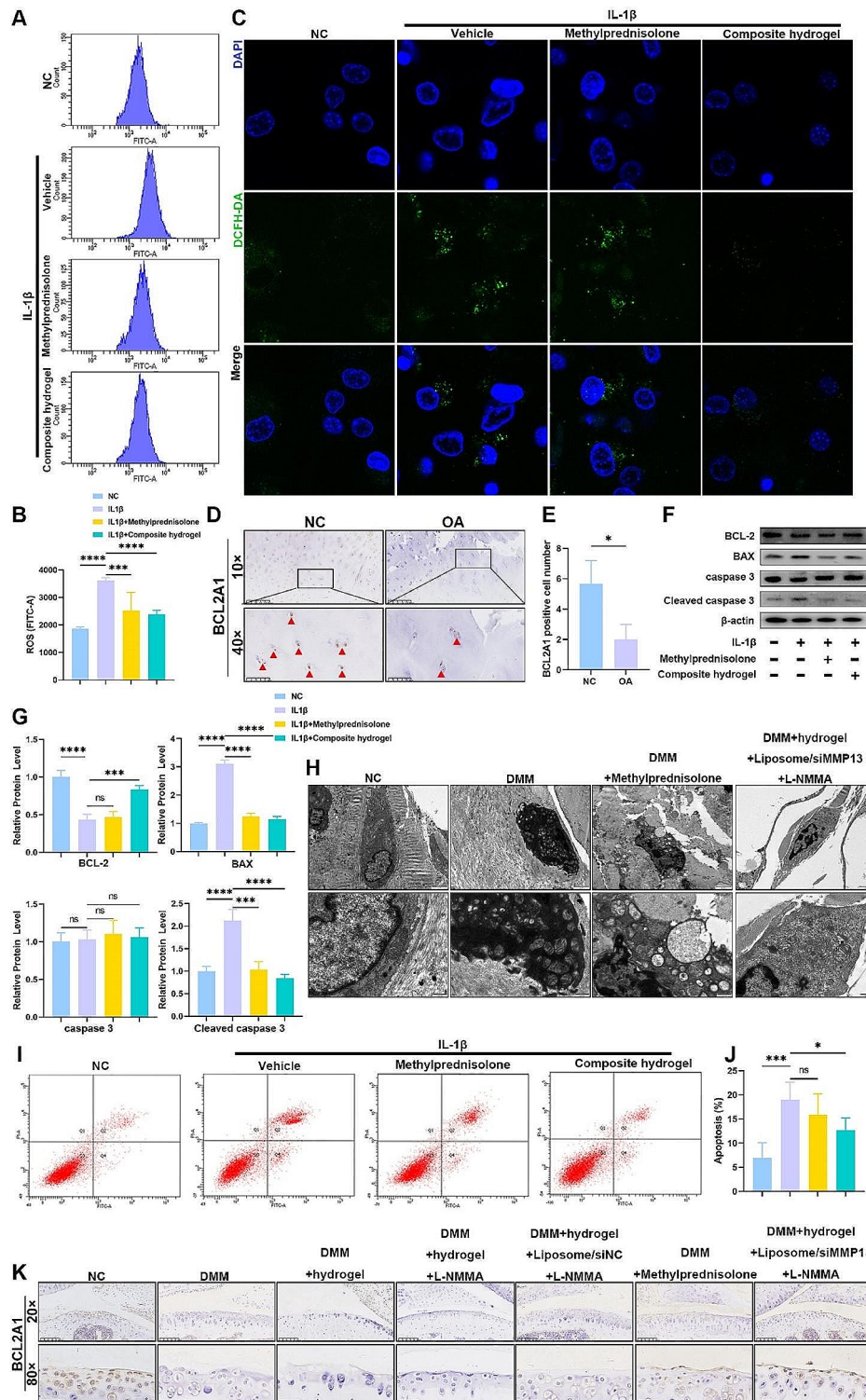


Fig. 8 (A) Total ROS levels are analyzed by flow cytometry. Quantitative analysis presented in (B) ($n=6$). (C) DCFH-DA staining of the intracellular ROS generation. (D) Representative IHC of BCL2A1 from human issues of OA patients and non-OA patients. Scale bar, 50 μ m (10 \times), 200 μ m (40 \times). Quantitative analysis presented in (E) ($n=3$). (F) WB of BCL-2, BAX, caspase3, cleaved-caspase3, and β -actin. Quantitative analysis presented in (G) ($n=4$). (H) Representative scanning electron microscope images of chondrocytes. (I) Cell apoptosis was analyzed by flow cytometry. Quantitative analysis presented in (J) ($n=6$). (K) Representative IHC staining of BCL2A1 from the knee joint of mice in different groups. (ns, no significance, * $P < 0.05$, ** $P < 0.01$, *** $P < 0.005$, **** $P < 0.001$)

potential for inhibiting the expression of key mediators involved in cartilage degradation, such as MMP13. Through the specific downregulation of MMP13 and other disease-relevant targets, RNAi therapy aims to mitigate cartilage breakdown and preserve joint integrity. This study targeted MMP13 and utilized the principles of RNA interference therapy to deliver siMMP13 into chondrocytes, suppressing its expression. This ensured the stability of cartilage matrix anabolism and catabolism. Both in vivo and in vitro experiments demonstrated promising therapeutic effects.

Furthermore, the development of advanced delivery systems, such as liposome-encapsulated siRNA and hydrogel formulations, enhances the efficacy and safety of RNAi therapy, paving the way for its clinical translation as a novel treatment strategy for OA. Currently, numerous studies are dedicated to developing such biomaterials, including extracellular vesicles, natural cell membranes, the application of photoporation, and others, all of which have achieved significant advancements [55, 56]. Simultaneously, the synthesis and application of various novel hydrogels provide an excellent carrier for biomaterials, enhancing their efficacy [57, 58]. The results of our research demonstrated that liposomes exhibit significantly greater hydrodynamic behavior in a colloidal state compared to a solid state, and the positive charge on the surface of the liposomes facilitates the cellular uptake of siMMP13. Furthermore, our designed F127/HAPBA hydrogel exhibited excellent thermosensitive characteristics. As the temperature changed, the hydrogel demonstrated favorable solid properties and elasticity. Additionally, the shear viscosity of the F127/HAPBA hydrogel met the standards required for intra-articular injection hydrogels and showed an appropriate degradation rate. These findings indicate that the composite hydrogel is an ideal carrier for intra-articular injections.

However, it is imperative to acknowledge certain limitations inherent in this experimental approach. For instance, the animal study failed to incorporate a temporal gradient, thus precluding a nuanced understanding of the treatment's time-dependent effects. Additionally, the oversight regarding the biodegradation kinetics of the material within the knee joint is noteworthy and requires careful consideration in future iterations. To address these methodological gaps comprehensively, our forthcoming investigations will prioritize the development of meticulously tailored designs. Specifically, we aim to explore specialized strategies targeting type 2 collagen, a pivotal constituent of articular cartilage, in order to optimize treatment efficacy and longevity.

Conclusion

To sum up, this study developed a composite RNA interference therapy. This therapy targeted MMP13, employing nanocarrier liposomes to encapsulate MMP13-specific siRNA, along with a thermosensitive hydrogel and the ROS inhibitor L-NMMA. Notably, this approach demonstrated no apparent biological toxicity, showcasing excellent biocompatibility. In vitro experiments revealed the composite therapy's superior ability to penetrate chondrocytes, significantly suppressing MMP13 expression and demonstrating strong resistance against ROS, apoptosis, and inflammation. Subsequent in vivo experiments in animal models indicated that this composite therapy effectively reduced matrix metalloproteinase levels within the knee joint cavity and alleviated cartilage degeneration. It safeguarded the normal synthesis of cartilage matrix, protecting the knee joint's structural integrity and thereby slowing down the progression of osteoarthritis. Additionally, transcriptomic sequencing identified the involvement of the PI3K-Akt signaling pathway, and subsequent validation confirmed that the therapeutic effects of the composite therapy are mediated through this pathway. Compared to current osteoarthritis treatments, this composite therapy exhibits high target specificity, minimal side effects, diverse mechanisms, and simple operability. These characteristics provide a novel perspective for future clinical osteoarthritis treatment, offering innovative possibilities for patients with osteoarthritis.

Methods and materials

Synthesis and physicochemical characterization

mPEG-PLGA was purchased from Ponsure Biological (Shanghai, China). DOTAP (1,2-Dioleoyl-3-trimethylammonium-propane chloride) and 3-aminophenylboronic acid were purchased from Macklin Biochemical Co. (Shanghai, China). Sodium Hyaluronate was purchased from Bloomage BioTechnology Corporation Limited. Pluronic F-127 and DMTMM (4-(4,6-Dimethoxy-1,3,5-triazin-2-yl)-4-methylmorpholin-4-ium chloride) were purchased from Sigma-Aldrich (America).

In brief, 1 μ M siMMP13 RNA was dissolved in 25 μ L RNA-Free water, emulsified by ultrasound for 1 min. mPEG-PLGA and DOTAP dissolved in 0.5 mL of chloroform solution. Mixed above solution to obtain the initial emulsion and added it dropwise to 5 mL RNA-Free water for ultrasonic emulsification. Finally, concentrate to 1 mL on a rotary evaporator to obtain the final product liposome. For measure the loading efficiency of siMMP13 in liposome, we customized the si-MMP3-FAM in GenePharma company to quantify detection of siMMP13 in liposome by utilizing the characteristics of FAM.

$$\text{Loading Efficiency} = \frac{\text{Weight of loaded siMMP13} - \text{FAM}}{\text{Weight of initially added siMMP13} - \text{FAM}} \times 100\%$$

HAPBA was synthesized using the method described in Gao's work [45]. Briefly, 100 mg hyaluronic acid (HA) was dissolved in 20 mL pure water. Then added 47 mg of 3-aminophenylboronic acid and 80 mg of DMTMM to the solution, adjusted pH to 6.5 and stirred for 3 days at room temperature. After the solution was dialysed in the 6–8 K dialysis tubing for 4 days, the final product was obtained by freeze-drying.

The morphologies of siMMP13 liposome were observed on a transmission electron microscope TECNAI12 (PHILIPS, Holland) at 120 kV acceleration voltage. The particle sizes and zeta potentials of the prepared siMMP13 liposome were obtained by a Malvern Zetasizer (NanoZS90, Westborough, MA). Fourier-transformed infrared spectroscopy (FTIR) spectra of HA and HA-PBA were performed on a Nicolet iS-50 FTIR Spectrometer (Thermo Scientific, USA) and collected in a mid-IR range (4000–400 cm^{-1}). To detect the degree of substitution of HAPBA, proton nuclear magnetic resonance (^1H NMR, Qone AS400.) measurements were performed, and the degree of PBA substitution in HA-PBA was calculated as the following equation.

$$DS_{(PBA)} = \frac{\text{Area}(7.89 \text{ ppm}) + \text{Area}(7.68 \text{ ppm}) + \text{Area}(7.62 \text{ ppm}) + \text{Area}(7.49 \text{ ppm})}{\text{Area}(1.9 \text{ ppm})} \times \frac{3}{4} \times 100\%$$

Rheological tests of hydrogels

All rheological characterizations were performed on a TA rheometer (MCR92, Anton Paar GmbH, Austria). Each sample was uniformly loaded between the plate of rheometer and the plate clamp with a diameter of 25 mm was used. Gelation temperature was determined by measuring the storage modulus (G') and loss (G'') of hydrogel in temperature sweep mode. The shear viscosity of hydrogels was measured in continuous flow with shear rates from 0.01 to 1000 s^{-1} . The viscosity of the gel phase was also investigated at constant temperature by flow sweep. The amplitude was fixed at 1% and the frequency from 0.01 to 100 Hz at 25 ± 0.2 °C to plot the data of the frequency sweep.

In vitro degradation tests

Hydrogels were prepared in a circular mold with a diameter of 10 mm and a height of 2 mm. The prepared hydrogels were then immersed in DPBS, and replaced DPBS every 24 h. The weight of the hydrogel was recorded as W_0 under dry condition, and the weight weighed at 0 h, 2 h, 4 h, 6 h, 8 h, 24 h, 2 d, 3 d was recorded as W . The

degradation rate of the hydrogel was calculated according to the following equation, and 3 samples are measured in each group.

$$D_s = \left(1 - \frac{W}{W_0}\right) \times 100\%$$

siMMP13 release from hydrogel

F127/HAPBA/liposome-siMMP13-FAM hydrogel was prepared in circular molds with a diameter of 10 mm and a height of 2 mm, and 3 samples were prepared per group; The hydrogel was merged in 1 mL DPBS, shaker at 37 °C, 90 rpm. The samples were taken at 1 h, 4 h, 8 h, 24 h, 36 h, 48 h and 72 h, respectively. The absorbance of the collected sample was measured by F127/HAPBA/liposome-siMMP13-FAM hydrogel was prepared in circular molds with a diameter of 10 mm and a height of 2 mm, and 3 samples were prepared per group; The hydrogel was merged in 1 mL DPBS, shaker at 37 °C, 90 rpm. The samples were taken at 1 h, 4 h, 8 h, 24 h, 36 h, 48 h and 72 h, respectively. The absorbance of the collected sample was measured by SpectraMax 190 excited at 494 nm and emitted at 519 nm to calculate the release of siMMP13-FAM.

Patient tissue samples

This study involved the collection of human knee-joint tissue samples from patients undergoing knee surgery. The Ethics Committee of the Sir Run Run Shaw Hospital approved this research, and informed consent was obtained from all patients and their relatives prior to the surgeries. We categorized the collected samples into two groups: one group consisted of patients with OA, while the non-OA patients served as a control group. The tissue samples were fixed in 4% paraformaldehyde at 4 °C for 48 h in preparation for further experiments.

Osteoarthritis modeling

Using adult male C57 mice as the research subjects, medial meniscal destabilization (DMM) surgery was performed (7 groups, $n=10$, 8 weeks old, average weight=20 g). After anesthesia, the knee skin is exposed by removing the hair near the knee joint. A surgical blade is then used to cut the skin to expose the joint cavity. Then curved forceps were used on the side to free muscles and ligaments, avoiding damage to the patellar ligament. Subsequently, the medial meniscal ligament was cut with pointed scissors. The medial meniscus was then damaged with pointed forceps and removed, ensuring to avoid damage to the articular cartilage. Finally, the skin was closed and the incision was sutured. The NC group only involved opening the joint cavity without removing the meniscus. All animal experiments were conducted

according to the protocol approved by The Ethics Committee of the Sir Run Run Shaw Hospital.

Intra-articular injection

After one week of DMM modeling, mice were anesthetized and placed in a supine position. The knee joint was flexed at a 90° angle. After disinfecting with an iodine swab, a microsyringe was used to inject vertically into the skin, gently rotating to enter the joint cavity, avoiding damage to the articular cartilage. Each joint cavity was injected with 10 μ L drug, and then the needle was slowly withdrawn, applying pressure with an iodine swab to stop bleeding. The NC group and DMM group were injected with saline, while the other groups were injected with the corresponding treatment compounds. Drug preparation was performed on ice.

Animal imaging in vivo

The in vivo imaging in this experiment was based on the PerkinElmer system (USA). Twenty-four hours prior to the detection time, the IVISense MMP 680 Fluorescent Probe (MMPsense) was injected into the joint cavity. The following day, mice were anesthetized and positioned in the IVIS Lumina XRMS system for live bioluminescence imaging.

Extraction and culture of mouse chondrocytes

Samples of knee cartilage were obtained from 5-day-old C57/BL6 suckling male mice immediately after euthanasia. The cartilage specimens underwent a comprehensive rinsing procedure using salt solution (HANK, Gibco, USA) and were subsequently fragmented. These fragments were then exposed to a 24-hour digestion process utilizing 0.2% type-2 collagenase (Sigma, USA). The next day, the resultant mixture underwent filtration through a 100 μ m cell strainer. Following a double wash with HANK, the segregated cells were cultured in a 5% CO₂, 37 °C incubator using a complete culture medium comprising DMEM (Gibco, Invitrogen, USA), supplemented with 10% FBS (Gibco, Invitrogen, USA), and antibiotics. The culture medium underwent renewal every 2–3 days to facilitate optimal cell growth and ensure maintenance.

High density chondrocytes culture in vitro

Chondrocytes were seeded in a six-well plate (Corning, USA), and different treatment measures, such as IL-1 β (Proteintech, China), siRNA (Ribobio, China), RNAi max (Invitrogen, USA), methylprednisolone (MCE, China), and composite hydrogel, were added according to different groups. The plates were then placed in a cell culture incubator and cultured for 48 h. Subsequently, the cells were digested, centrifuged at 800 rounds per minute for 5 min, the supernatant was aspirated using a pipette, resuspended in 20 μ L of culture medium, and

then vertically dropped in the center of a 12-well plate. The plate was placed back into the cell culture incubator for 2 h to allow cell attachment. After 2 h, an appropriate amount of culture medium was slowly added along the wall using a pipette, taking care not to disperse the adherent cells. The plate was then returned to the cell culture incubator and cultured for an additional 48 h. Following this, the plate was taken out, the supernatant was aspirated, and the wells were washed three times with sterile Phosphate Buffer Saline (PBS, Cellmax, China) solution. Staining was performed using Safranin O, Alcian Blue, and Toluidine Blue at room temperature for 2 h. After aspirating the staining solution, the wells were rinsed, and imaging was conducted.

Micro-CT analysis

The knee joint was removed after the mice were euthanized. After immersing the knee joint of mice in 4% paraformaldehyde for 48 h at room temperature, we conducted imaging using a dedicated micro-CT scanner (model: Skyscan 1275, Aartselaar, Belgium). The imaging process employed an X-ray with settings at 60 μ A/50 kV, producing a resolution of 9 μ m.

Western blotting

Protein extraction involved treating the samples with RIPA lysis buffer containing phosphatase and protease inhibitors (Beyotime, China). The resulting proteins were separated using SDS-PAGE gel electrophoresis, followed by transfer onto PVDF membranes for subsequent analysis. After blocking with 5% bovine serum albumin (BSA) at room temperature for 60 min, PVDF membranes were appropriately cut based on the molecular weight of target proteins and incubated with primary antibodies for 12 h. Primary antibodies used included aggrecan (#ET1704-57, Huabio, China, 1:1000), Sox9 (#ET1611-56, Huabio, China, 1:1000), Col2 (#ER1906-48, Huabio, China, 1:1000), MMP3 (#ET1705-98, Huabio, China, 1:1000), MMP13 (#ab219620, Abcam, UK, 1:1000), Adamts5 (#HA722011, Huabio, China, 1:1000), PI3K (#ab191606, Abcam, UK, 1:1000), p-PI3K (#ab182651, Abcam, UK, 1:1000), AKT (#ab179463, Abcam, UK, 1:1000), p-AKT (#ab192623, Abcam, UK, 1:1000), p38 (#ab170099, Abcam, UK, 1:1000), p-p38 (#ab4822, Abcam, UK, 1:1000), Jnk (#ab179461, Abcam, UK, 1:1000), p-Jnk (#ab124956, Abcam, UK, 1:1000), Erk (#ET1601-29, Huabio, China, 1:1000), p-Erk (#ET1610-13, Huabio, China, 1:1000), BCL-2 (#ET1603-11, Huabio, China, 1:1000), BAX (#ET1603-34, Huabio, China, 1:1000), caspase3 (#9662S, CST, USA, 1:1000), cleaved-caspase3 (#9661, CST, USA, 1:1000), iNOS (#ab178945, Abcam, UK, 1:1000), TNF- α (#ab183218, Abcam, UK, 1:1000), and β -actin (#EM21002, Huabio, China, 1:1000). HRP-linked secondary antibodies, including anti-rabbit IgG

HRP-linked antibody (#7074S, CST, USA, 1:5000), and anti-mouse IgG HRP-linked antibody (#7076S, CST, USA, 1:5000), were then incubated with the membranes. Chemiluminescence reagents from Amersham Biosciences (Buckinghamshire, USA) were used to capture the protein bands.

RNA isolation and real-time quantitative PCR

Total RNA extraction from the respective groups was carried out using the TRIZOL reagent (Invitrogen, USA). The concentration and purity of the RNA samples were determined using the NanoDrop 2000 spectrophotometer. Reverse transcription was performed on the RNA samples using the PrimeScript RT MasterMix (Yeason, China) to facilitate the synthesis of complementary DNA (cDNA). Real-time quantitative polymerase chain reaction (RT-qPCR) was employed for assessing mRNA levels, utilizing the SYBR Green qPCR Master Mix (Yeason, China). The RT-qPCR reactions involved an initial denaturation step at 95 °C for 5 min, followed by 40 cycles of amplification (95 °C for 15 s and 60 °C for 60 s), and a final melting curve analysis (95 °C for 15 s and 60 °C for 60 s). To ensure reproducibility and statistical reliability, RT-qPCR experiments were conducted in triplicate. The mRNA expression levels were normalized to the internal control gene β -actin. The primer sequences employed in the experiments are available in Table 1

Elisa analysis

The Elisa kits performed in this experiment were purchased from Lianke Bio (China) and were operated in strict accordance with the instructions, and all experiments were repeated at least three times.

Flow cytometry

All Flow cytometry involved in this study were performed by professional technicians using a FACSCalibur

(BD, USA) in strict accordance with the guidelines, and all were repeated at least three times.

Tissue-specific staining

Mice knee joints were dissected to specimens. These specimens underwent fixation in 4% paraformaldehyde (4 °C, 48 h) and were subsequently decalcified using EDTA for a duration of 14 days. Following decalcification, the specimens underwent sequential dehydration, paraffin embedding, and sectioning into slices of 5 μ m thickness. To prepare the sections for histology and immunohistochemistry, the slices were deparaffinized with xylene, followed by rehydration using step concentrations of ethanol solutions. Subsequently, standard protocols were employed for staining, utilizing techniques such as H&E, Alcian Blue, Masson, Safranin O/Fast green to visualize specific tissue features.

Immunohistochemistry staining

The sections mentioned above underwent treatment with H₂O₂ (3%) for 20 min to block endogenous peroxidase activity. Subsequently, trypsin incubation was performed for 20 min, followed by blocking of unspecific antigens using a solution containing 1% Tween-20 and 5% bovine serum albumin in PBS for 60 min. The sections were then incubated with primary antibodies overnight at a temperature of 4 °C. The antibodies used included Sox9 (#ET1611-56, Huabio, China, 1:200), MMP13 (#ab219620, Abcam, UK, 1:200), and MMP3 (#ab52915, Abcam, China, 1:200). Corresponding secondary antibodies conjugated to HRP (CST, 1:5000) were applied to the sections. Following this, the sections were counterstained with hematoxylin. Quantification of positive cells was carried out by capturing images of 6 random fields at a magnification of 100 \times using Image J software. Cell quantification was independently performed by three researchers.

Immunofluorescence staining

The sections underwent blocking with 5% BSA for 60 min, followed by a 12-hour incubation at 4 °C with primary antibodies against Col2 (#ab307674, Abcam, UK, 1:200). After washing, the sections were incubated for 60 min at room temperature with anti-rabbit Alexa Fluor (488) secondary antibody (#710369, Invitrogen, US, 1:300). DAPI (#D9542, Sigma-Aldrich, US) was used to stain the nuclei (0.1 μ g/mL, 30 min, room temperature). Histological scoring and quantitative analysis of immunofluorescence staining were conducted in a double-blinded manner to minimize bias.

Transmission electron microscopy

Tissue sampling and fixation were initiated by taking approximately 1–2 mm³ of tissue, treating it with 2.5%

Table 1 Specific primer sequences for RT-qPCR

Gene	F (5'-3')	R (5'-3')
β -actin	AGCCATGTACGTAGCCATCC	CTCTCAGCTGT GGTGGTGAA
aggrecan	TTGACAGACATTGACGAGTGC	TTAGTCCACCC CTCCTCACA
Sox9	TGAAGATGACCGACGAGCAG	GGATGCACACG GGGAACTTA
MMP13	CTTCTGGCACACGCTTTTCC	ATGGGAAACAT CAGGGCTCC
MMP3	GGAGGCAGCAGAGAACCTAC	AGGACCGGAA GACCCTTCAT
iNOS	GGTGAAGGGACTGAGCTGTTA	TGAAGAGAAAC TTCCAGGGGC
TNF- α	ATGGCCTCCCTCATCAGT	TTTGCTACGAC GTGGGCTAC

glutaraldehyde, and storing it at 4 °C. Osmic acid fixation followed, involving a triple rinse with 0.1 M phosphate buffer (pH 7.4) and a 2 h fixation using 1% osmic acid at room temperature. Dehydration ensued through a series of alcohol concentrations, and permeation was achieved using acetone: epoxy resin combinations. The embedding phase involved placing the permeated sample in an embedding plate with epoxy resin and polymerizing it at 60 degrees for 48 h. Ultra-thin microtome slices (80–100 nm) were obtained, followed by double staining with uranium and lead. The sections were then dried and observed under electron microscopy (Thermo Fisher Scientific, USA) after staining.

Statistical analysis

The data were presented as mean ± standard deviation (SD) with individual data points. Statistical analysis was conducted using SPSS 19.0 (SPSS, Chicago). The normal distribution of the data was assessed using the Shapiro-Wilk test. For normally distributed data, Student's *t*-test, one-way ANOVA, and Tukey's post hoc analysis were employed to evaluate statistical differences between groups. Nonparametric tests were utilized for non-normally distributed data. A significance level of $P < 0.05$ was considered statistically significant. To ensure robustness and reproducibility, all experiments were independently conducted at least three times.

Abbreviations

OA	Osteoarthritis
RNAi	RNA interference
ROS	Reactive oxygen species
ECM	Extracellular matrix
MMP13	Matrix metalloproteinases 13
L-NMMA	NG-Monomethyl-L-arginine Acetate
IL-6	Interleukin 6
IL-1β	Interleukin 1β
Col2	type II collagen
Sox9	SRY sex determining region Y-box 9
DMOADs	Disease-modifying OA drugs
PTOA	Post-traumatic osteoarthritis
DLS	Dynamic light scattering
NOS	Nitric oxide synthase
MP	Methylprednisolone
DMM	Destabilization of the medial meniscus
TNF-α	Tumor necrosis factor-alpha
IHC	Immunohistochemistry
IF	Immunofluorescence

Supplementary Information

The online version contains supplementary material available at <https://doi.org/10.1186/s12951-024-02740-w>.

Supplementary Material 1

Acknowledgements

We thank Xiaoli Hong from the Core Facilities, Zhejiang University school of Medicine for their technical support.

Author contributions

Zhongyin Ji, Xiaobin Ren, Jiayan Jin, Xin Ye, Hao Yu, Wenhan Fang, Hui Li, Yihao Zhao, Siyue Tao, Xiangxi Kong, Jiao Cheng, Zhi Shan, Jian Chen, Qingqing Yao, Fengdong Zhao and Junhui Liu. Z. J.: Writing—original draft; Project administration. X. R.: Methodology; Project administration. J. J.: Project administration; Writing—review & editing. X. Y.: Methodology; Project administration. H. Y.: Project administration. W. F.: Methodology; Project administration. H. L.: Methodology; Project administration. Y. Z.: Project administration. S. T.: Project administration. X. K.: Project administration. J. C.: Writing—review & editing. Z. S.: Founding. J. C.: Resources; Writing—review & editing. Q. Y.: Data curation; Supervision; F. Z.: Supervision; Writing—review & editing. J. L.: Conceptualization; Formal analysis; Supervision; Funding acquisition; Writing—review & editing.

Funding

This study was supported by the National Natural Science Foundation of China (Grant No. 82272521), Zhejiang Provincial Natural Science Foundation of China (Grant No. LZ23H060002, LGD22H060002), Zhejiang Medical Science and Technology Project (Grant No. 2023564481).

Data availability

All data needed to evaluate the conclusions in the paper are present in the paper and/or the Supplementary Materials. Additional data related to this paper are available from the authors upon reasonable request.

Declarations

Ethical approval

All animal experiments were approved by the ethics committee of Zhejiang University, which followed the Guidelines for Care and Use of Laboratory Animals from National Institutes of Health. All the human tissues involved in this study have been authorized by patients' signature and approved by the ethics committee of Sir Run Run Shaw Hospital.

Consent for publication

Not applicable.

Conflict of interest

The authors do not have competing interests to declare.

Author details

¹Department of Orthopaedic Surgery, Sir Run Run Shaw Hospital, Zhejiang University School of Medicine, No. 3, Qingchun Road East, Hangzhou 310016, P.R. China

²School of Ophthalmology & Optometry, Eye Hospital, Wenzhou Medical University, 270 Xueyuan Xi Road, Wenzhou 325027, Zhejiang, P.R. China

³Key Laboratory of Musculoskeletal System Degeneration and Regeneration Translational Research of Zhejiang Province, No. 3, Qingchun Road East, Hangzhou 310016, P.R. China

⁴College of Laboratory Medicine and Life sciences, Wenzhou Medical University, Wenzhou 325035, Zhejiang, P.R. China

⁵Department of Orthopedics Surgery, Peking Union Medical College Hospital, Chinese Academy of Medical Sciences and Peking Union Medical College, Beijing 100730, P.R. China

Received: 12 April 2024 / Accepted: 24 July 2024

Published online: 02 August 2024

References

1. Barnett R. Osteoarthritis. *Lancet* (London England). 2018;391:1985.
2. Martel-Pelletier J, Barr AJ, Cicuttini FM, Conaghan PG, Cooper C, Goldring MB, et al. Osteoarthritis. *Nat Reviews Disease Primers*. 2016;2:16072.
3. Prieto-Alhambra D, Judge A, Javadi MK, Cooper C, Diez-Perez A, Arden NK. Incidence and risk factors for clinically diagnosed knee, hip and hand osteoarthritis: influences of age, gender and osteoarthritis affecting other joints. *Ann Rheum Dis*. 2014;73:1659–64.
4. Scanzello CR, Goldring SR. The role of synovitis in osteoarthritis pathogenesis. *Bone*. 2012;51:249–57.

5. Bálint G, Szebenyi B. Diagnosis of osteoarthritis. Guidelines and current pitfalls. *Drugs*. 1996;52(Suppl 3):1–13.
6. Felson DT, Lawrence RC, Dieppe PA, Hirsch R, Helmick CG, Jordan JM, et al. Osteoarthritis: new insights. Part 1: the disease and its risk factors. *Ann Intern Med*. 2000;133:635–46.
7. Dieppe PA, Lohmander LS. Pathogenesis and management of pain in osteoarthritis. *Lancet* (London England). 2005;365:965–73.
8. Reyes C, Leyland KM, Peat G, Cooper C, Arden NK, Prieto-Alhambra D. Association between Overweight and Obesity and risk of clinically diagnosed knee, hip, and Hand Osteoarthritis: a Population-based Cohort Study. Volume 68. *Hoboken, NJ: Arthritis & rheumatology*; 2016. pp. 1869–75.
9. Takahashi N, Rieneck K, van der Kraan PM, van Beuningen HM, Vitters EL, Bendtsen K, et al. Elucidation of IL-1/TGF-beta interactions in mouse chondrocyte cell line by genome-wide gene expression. *Osteoarthr Cartil*. 2005;13:426–38.
10. Hu Q, Ecker M. Overview of MMP-13 as a Promising Target for the treatment of Osteoarthritis. *Int J Mol Sci*. 2021; 22.
11. Mehana EE, Khafaga AF, El-Blehi SS. The role of matrix metalloproteinases in osteoarthritis pathogenesis: an updated review. *Life Sci*. 2019;234:116786.
12. Loeser RF. Osteoarthritis year in review 2013: biology. *Osteoarthr Cartil*. 2013;21:1436–42.
13. Tanamas S, Hanna FS, Cicuttini FM, Wluka AE, Berry P, Urquhart DM. Does knee malalignment increase the risk of development and progression of knee osteoarthritis? A systematic review. *Arthritis Rheum*. 2009;61:459–67.
14. Eichaker LR, Cho H, Duvall CL, Werfel TA, Hasty KA. Future nanomedicine for the diagnosis and treatment of osteoarthritis. *Nanomed* (London England). 2014;9:2203–15.
15. O'Grady KP, Kavanaugh TE, Cho H, Ye H, Gupta MK, Madonna MC, et al. Drug-free ROS sponge polymeric microspheres reduce tissue damage from ischemic and mechanical injury. *ACS Biomaterials Sci Eng*. 2018;4:1251–64.
16. Richette P, Poitou C, Garnero P, Vicaud E, Bouillot JL, Lacorte JM, et al. Benefits of massive weight loss on symptoms, systemic inflammation and cartilage turnover in obese patients with knee osteoarthritis. *Ann Rheum Dis*. 2011;70:139–44.
17. Issa SN, Sharma L. Epidemiology of osteoarthritis: an update. *Curr Rheumatol Rep*. 2006;8:7–15.
18. McAlindon TE, Bannuru RR, Sullivan MC, Arden NK, Berenbaum F, Bierma-Zeinstra SM, et al. OARSI guidelines for the non-surgical management of knee osteoarthritis. *Osteoarthr Cartil*. 2014;22:363–88.
19. Sterner B, Harms M, Wöll S, Weigandt M, Windbergs M, Lehr CM. The effect of polymer size and charge of molecules on permeation through synovial membrane and accumulation in hyaline articular cartilage. *Eur J Pharm Biopharmaceutics: Official J Arbeitsgemeinschaft für Pharmazeutische Verfahrenstechnik eV*. 2016;101:126–36.
20. Cho H, Stuart JM, Magid R, Danila DC, Hunsaker T, Pinkhassik E et al. Theranostic immunoliposomes for osteoarthritis. *Nanomedicine: nanotechnology, biology, and medicine*. 2014 10: 619–27.
21. Larsen C, Ostergaard J, Larsen SW, Jensen H, Jacobsen S, Lindegaard C, et al. Intra-articular depot formulation principles: role in the management of postoperative pain and arthritic disorders. *J Pharm Sci*. 2008;97:4622–54.
22. Rothenfluh DA, Bermudez H, O'Neill CP, Hubbell JA. Biofunctional Polymer nanoparticles for intra-articular targeting and retention in cartilage. *Nat Mater*. 2008;7:248–54.
23. McAlindon TE, LaValley MP, Harvey WF, Price LL, Driban JB, Zhang M, et al. Effect of intra-articular triamcinolone vs saline on knee cartilage volume and Pain in patients with knee osteoarthritis: a Randomized Clinical Trial. *JAMA*. 2017;317:1967–75.
24. Zhou F, Zhang X, Cai D, Li J, Mu Q, Zhang W, et al. Silk fibroin-chondroitin sulfate scaffold with immuno-inhibition property for articular cartilage repair. *Acta Biomater*. 2017;63:64–75.
25. Beavers KR, Nelson CE, Duvall CL. MiRNA inhibition in tissue engineering and regenerative medicine. *Adv Drug Deliv Rev*. 2015;88:123–37.
26. Nelson CE, Kintzing JR, Hanna A, Shannon JM, Gupta MK, Duvall CL. Balancing cationic and hydrophobic content of PEGylated siRNA polyplexes enhances endosome escape, stability, blood circulation time, and bioactivity in vivo. *ACS Nano*. 2013;7:8870–80.
27. Mazur CM, Woo JJ, Yee CS, Fields AJ, Acevedo C, Bailey KN, et al. Osteocyte dysfunction promotes osteoarthritis through MMP13-dependent suppression of subchondral bone homeostasis. *Bone Res*. 2019;7:34.
28. Wang M, Sampson ER, Jin H, Li J, Ke QH, Im HJ, et al. MMP13 is a critical target gene during the progression of osteoarthritis. *Arthritis Res Therapy*. 2013;15:R5.
29. Jackson MA, Werfel TA, Curvino EJ, Yu F, Kavanaugh TE, Sarett SM, et al. Zwitterionic Nanocarrier Surface Chemistry improves siRNA tumor delivery and silencing activity relative to polyethylene glycol. *ACS Nano*. 2017;11:5680–96.
30. Vaidya T, Agrawal A, Mahajan S, Thakur MH, Mahajan A. The Continuing evolution of Molecular Functional Imaging in Clinical Oncology: the Road to Precision Medicine and Radiogenomics (Part I). *Mol Diagn Ther*. 2019;23:1–26.
31. Ruan MZ, Erez A, Guse K, Dawson B, Bertin T, Chen Y, et al. Proteoglycan 4 expression protects against the development of osteoarthritis. *Sci Transl Med*. 2013;5:176ra34.
32. Krzeski P, Buckland-Wright C, Bálint G, Cline GA, Stoner K, Lyon R, et al. Development of musculoskeletal toxicity without clear benefit after administration of PG-116800, a matrix metalloproteinase inhibitor, to patients with knee osteoarthritis: a randomized, 12-month, double-blind, placebo-controlled study. *Arthritis Res Therapy*. 2007;9:R109.
33. Chen K, Chen X. Integrin targeted delivery of chemotherapeutics. *Theranostics*. 2011;1:189–200.
34. Clutterbuck AL, Asplin KE, Harris P, Allaway D, Mobasher A. Targeting matrix metalloproteinases in inflammatory conditions. *Curr Drug Targets*. 2009;10:1245–54.
35. Sarett SM, Werfel TA, Chandra J, Jackson MA, Kavanaugh TE, Hattaway ME, et al. Hydrophobic interactions between polymeric carrier and palmitic acid-conjugated siRNA improve PEGylated polyplex stability and enhance in vivo pharmacokinetics and tumor gene silencing. *Biomaterials*. 2016;97:122–32.
36. Liu J, Khalil RA. Matrix metalloproteinase inhibitors as investigational and therapeutic tools in unrestrained tissue remodeling and pathological disorders. *Progress in molecular biology and translational science*. 2017 148: 355–420.
37. Kilchrist KV, Dimobi SC, Jackson MA, Evans BC, Werfel TA, Dailing EA, et al. Gal8 visualization of endosome disruption predicts carrier-mediated Biologic Drug Intracellular Bioavailability. *ACS Nano*. 2019;13:1136–52.
38. Settle S, Vickery L, Nemirovskiy O, Vidmar T, Bendele A, Messing D, et al. Cartilage degradation biomarkers predict efficacy of a novel, highly selective matrix metalloproteinase 13 inhibitor in a dog model of osteoarthritis: confirmation by multivariate analysis that modulation of type II collagen and aggrecan degradation peptides parallels pathologic changes. *Arthritis Rheum*. 2010;62:3006–15.
39. Jackson MA, Bedingfield SK, Yu F, Stokan ME, Miles RE, Curvino EJ, et al. Dual carrier-cargo hydrophobization and charge ratio optimization improve the systemic circulation and safety of zwitterionic nano-polyplexes. *Biomaterials*. 2019;192:245–59.
40. Werfel TA, Jackson MA, Kavanaugh TE, Kirkbride KC, Miteva M, Giorgio TD, et al. Combinatorial optimization of PEG architecture and hydrophobic content improves ternary siRNA polyplex stability, pharmacokinetics, and potency in vivo. *J Controlled Release: Official J Controlled Release Soc*. 2017;255:12–26.
41. Huang K, Lin Z, Ge Y, Chen X, Pan Y, Lv Z, et al. Immunomodulation of MiRNA-223-based nanoplatform for targeted therapy in retinopathy of prematurity. *J Controlled Release*. 2022;350:789–802.
42. Veider F, Sanchez Armengol E, Bernkop-Schnürch A. Charge-Reversible Nanoparticles: Advanced Delivery Systems for Therapy and Diagnosis. *Small* (Weinheim an der Bergstrasse, Germany). 2024; 20: e2304713.
43. Xu M, Qi Y, Liu G, Song Y, Jiang X, Du B. Size-dependent in vivo transport of nanoparticles: implications for delivery, targeting, and Clearance. *ACS Nano*. 2023;17:20825–49.
44. An H, Bo Y, Chen D, Wang Y, Wang H, He Y, et al. Cellulose-based self-healing hydrogel through boronic ester bonds with excellent biocompatibility and conductivity. *RSC Adv*. 2020;10:11300–10.
45. Gao H, Yu C, Li Q, Cao X. Injectable DMEM-induced phenylboronic acid-modified hyaluronic acid self-crosslinking hydrogel for potential applications in tissue repair. *Carbohydr Polym*. 2021; 258.
46. Wang M, Ye F, Wang H, Admassu H, Feng Y, Hua X, et al. Phenylboronic Acid Functionalized adsorbents for selective and reversible adsorption of lactulose from syrup mixtures. *J Agric Food Chem*. 2018;66:9269–81.
47. Ji M, Li P, Sheng N, Liu L, Pan H, Wang C, et al. Sialic acid-targeted nanovectors with Phenylboronic Acid-Grafted Polyethylenimine robustly enhance siRNA-Based Cancer Therapy. *ACS Appl Mater Interfaces*. 2016;8:9565–76.
48. von Lospichl B, Hemmati-Sadeghi S, Dey P, Dehne T, Haag R, Sittlinger M et al. Injectable hydrogels for treatment of osteoarthritis - A rheological study. *Colloids and surfaces B, Biointerfaces*. 2017; 159: 477–83.
49. Cai Z, Zhang H, Wei Y, Wu M, Fu A. Shear-thinning hyaluronan-based fluid hydrogels to modulate viscoelastic properties of osteoarthritis synovial fluids. *Biomaterials Sci*. 2019;7:3143–57.

50. Glasson SS, Blanchet TJ, Morris EA. The surgical destabilization of the medial meniscus (DMM) model of osteoarthritis in the 129/SvEv mouse. *Osteoarthr Cartil.* 2007;15:1061–9.
51. Li J, Zhang B, Liu WX, Lu K, Pan H, Wang T, et al. Metformin limits osteoarthritis development and progression through activation of AMPK signalling. *Ann Rheum Dis.* 2020;79:635–45.
52. Setten RL, Rossi JJ, Han SP. The current state and future directions of RNAi-based therapeutics. *Nat Rev Drug Discovery.* 2019;18:421–46.
53. Weng Y, Xiao H, Zhang J, Liang XJ, Huang Y. RNAi therapeutic and its innovative biotechnological evolution. *Biotechnol Adv.* 2019;37:801–25.
54. Lee JW, Choi J, Choi Y, Kim K, Yang Y, Kim SH, et al. Molecularly engineered siRNA conjugates for tumor-targeted RNAi therapy. *J Controlled Release: Official J Controlled Release Soc.* 2022;351:713–26.
55. Du H, Yin H, Qin Y, Min Y, Deng Q, Tan J, et al. Subcellular nanobionic liposome with High Zeta Potential enhances Intravesical Adhesion and Drug Delivery. *ACS Nano.* 2024;18:3583–96.
56. Wang L, Wei X, Liu H, Fan Y. Nanomaterial-mediated photoporation for intracellular delivery. *Acta Biomater.* 2023;157:24–48.
57. Li G, Liu S, Chen Y, Zhao J, Xu H, Weng J, et al. An injectable liposome-anchored teriparatide incorporated gallic acid-grafted gelatin hydrogel for osteoarthritis treatment. *Nat Commun.* 2023;14:3159.
58. Wang L, Wei X, He X, Xiao S, Shi Q, Chen P, et al. Osteoinductive Dental Pulp Stem Cell-Derived Extracellular vesicle-loaded multifunctional hydrogel for bone regeneration. *ACS Nano.* 2024;18:8777–97.

Publisher's Note

Springer Nature remains neutral with regard to jurisdictional claims in published maps and institutional affiliations.